Journal of Fluids and Structures 94 (2020) 102907

Contents lists available at ScienceDirect

Journal of Fluids and Structures

journal homepage: www.elsevier.com/locate/jfs

Making a splash with fabrics in hydrophilic sphere entry

Daren A. Watson, Chris J. Souchik, Madison P. Weinberg, Joshua M. Bom, Andrew K. Dickerson *

Department of Mechanical and Aerospace Engineering, University of Central Florida, United States of America

ARTICLE INFO

Article history:
Received 2 July 2019
Received in revised form 23 January 2020
Accepted 6 February 2020
Available online xxxx

Keywords:
Worthington jets
Cavity dynamics
Drag coefficient
Failure stress
Splash metrics
Water entry

ABSTRACT

Splash dynamics associated with impacts of solid projectiles into aqueous pools are traditionally investigated with respect to impactor geometry, velocity, and surface roughness. Fluid surface alteration in some instances, may be more easily accomplished for the tuning of splashes. In this combined experimental and theoretical study, smooth, free-falling, hydrophilic steel spheres impact a quiescent liquid pool for Weber numbers in the range of 430 − 2700. Spheres strike fabrics resting atop the fluid surface which are either punctured or remain intact. As spheres strike fabrics, flow separation is tripped at low speeds which would otherwise not produce air-entraining cavities. Punctured fabrics suppress splash crowns normally seen for cavity-producing impacts while intact fabrics generate deeper cavities, higher Worthington jets, and pronounced splash crowns. Some fabrics, both punctured and intact reduce drag with respect to clean surface impacts by providing the drag-reducing benefits of flow separation while not offering a high inertial penalty. Such observations augur well for interfacial fluid–structure interactions where splashes warrant control.

1. Introduction

The study of the hydrodynamics of free-falling projectiles into aqueous pools is relevant to real-life applications such as toilet dynamics, projectile water entry, and animal locomotion (Truscott and Techet, 2009; Hu et al., 2003; Watson et al., 2018). The water entry of such impactors often warrants control to mitigate unwanted exposure, but control of splashes and impactor deceleration in the milliseconds following surface contact is difficult due to limitations on impactor shape and entry dynamics. Numerous studies have followed the seminal work of Worthington (Worthington and Cole, 1897, 1900; Worthington, 1908), and traditionally investigate water entry physics in the context of impactor shape (Duclaux et al., 2007; Kubota and Mochizuki, 2011; Bodily et al., 2014), velocity (Duez et al., 2007), and surface roughness (Truscott et al., 2013; Li et al., 2019). One study considered the inclusion of a compliant solid interface atop the quiescent fluid surface during water entry. In Watson et al. (2018), we show the formation of air-entraining cavities at low impact velocities during hydrophilic sphere entry is triggered by the inclusion of thin, non-woven fabrics. Thin fabrics atop the fluid surface stymie upward fluid motion along the periphery of spheres and promote flow separation, which is analogous to an increase in water repellency. Inhibition of upward fluid motion along the body of spherical hydrophilic impactors transmutes the behavior of splash crowns and the resistance of fabric sheets to puncture, indicated by failure stress σ_f, influences air-entrainment as depicted in Fig. 1. When compared to the clean surface, inclusion of meager amounts of fabric amplifies Worthington jets and drag force for hydrophilic Delrin spheres.

* Corresponding author.
E-mail address: dickerson@ucf.edu (A.K. Dickerson).

https://doi.org/10.1016/j.jfluidstructs.2020.102907
0889-9746/

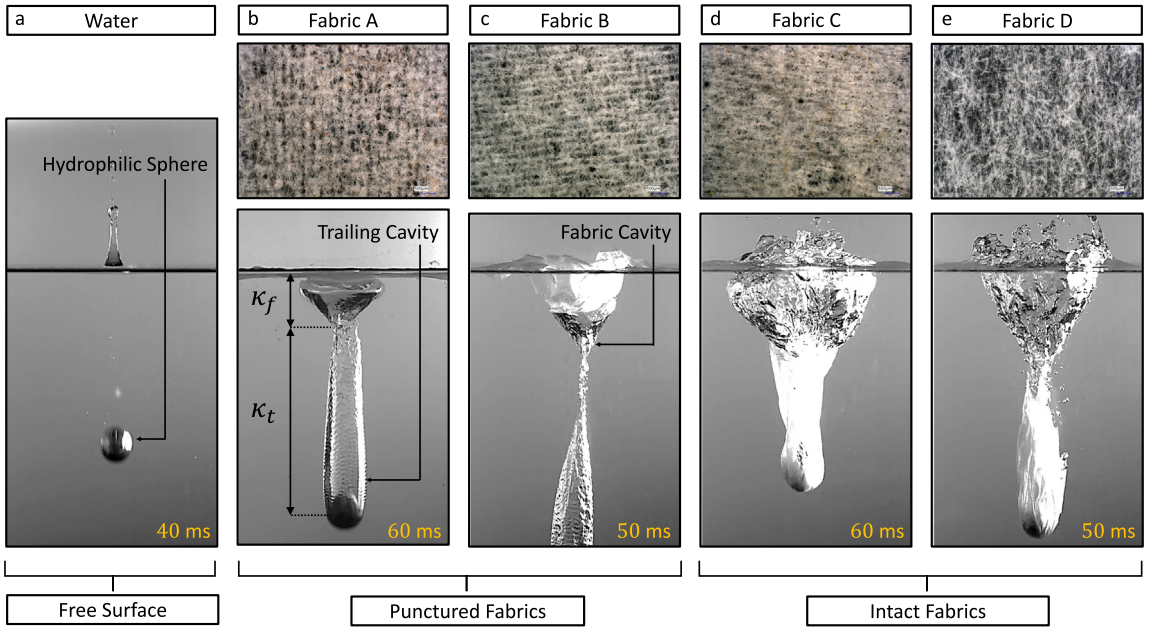

Fig. 1. Cavity formation and splash features for hydrophilic sphere impacts onto an aqueous pool with interfacial entry zone modified by (a) no fabric (b) Fabric A (c) Fabric B, (d) Fabric C, and (e) Fabric D. Fabric alters entry dynamics, producing air-entraining cavities below the critical threshold velocity $U \approx 8$ m/s required for hydrophilic spheres (Duez et al., 2007). Cavity depths are determined at the moment of seal between the fabric and trailing cavities. The fabric cavity depth is denoted by κ_f, and the length of the trailing cavity by κ_t. The top panel shows microscopic images of fabric weaves. The spheres pictured have diameter $D = 2.0$ cm, impact velocity $U = 3.13$ m/s, and We $= 2688$.

In the current study, we explore the splash and cavity dynamics of water entry by again employing thin fabrics atop the water surface to reveal the physics at the transition between fabrics which are punctured and those remaining intact after impacts within the range of Weber number We $= \rho U^2 D/\sigma = 430 - 2700$, where $\rho = 999$ kg/m^3 is the density of the fluid, D is the sphere diameter, U is the impact velocity, and $\sigma = 72.9$ mN/m is the surface tension of the fluid. This work moves beyond our previous study (Watson et al., 2018) by employing a wider variety of surface modification by fabric, and by connecting fabric material properties to entry dynamics. Here, punctured fabrics refer to those that are always torn by our impactors within the experimental range of We, while intact fabrics are not torn by impactors in our trials. Thus we relate splash dynamics to the resistance of fabrics to puncture. Our four chosen test fabrics are shown in Fig. 1.

The water entry of free-falling hydrophilic spheres show no flow separation or air-entrainment for impact velocities (Duez et al., 2007) below $U \approx 8$ m/s. In contrast, hydrophobic spheres begin to experience flow separation and air-entrainment at entry speeds $U < 8$ m/s, with the exact value a function of the impactors' hydrophobicity (Watson et al., 2018). The splashes resulting from the water entry of hydrophobic impactors consist of radial splash crowns (Cossali et al., 2004) and significantly higher Worthington jets compared to their hydrophilic counterparts (Watson et al., 2018). Such splash characteristics may be tuned by alteration of fluid viscosity (May, 1951; Cheny and Walters, 1996; Ogawa et al., 2006), surface tension (Castillo-Orozco et al., 2015; Che and Matar, 2018; Speirs et al., 2018), the fluid–solid density ratio (Truscott, 2009; Aristoff et al., 2010), impactor shape (Kubota and Mochizuki, 2011; Kim and Park, 2019), impactor wettability (Duez et al., 2007; Duck-Gyu and Ho-Young, 2008; Aristoff and Bush, 2009; Ueda and Iguchi, 2012; Zhao et al., 2016), impactor rotation (Truscott and Techet, 2009; Techet and Truscott, 2011) and entry velocity (Glasheen and McMahon, 1996; Thoroddsen et al., 2004; Duez et al., 2007). The first record of tuning a splash was made by Shin and McMahon (1990) who found that cavity interactions with the floor of a container may both amplify and attenuate the Worthington jet height. For liquid drop projectiles, they found splash heights were maximum when the pool depth is roughly 2X the impactor diameter. Cavities striking the fluid floor retract non-uniformly and attenuate splashing. Other studies varied fluid properties and showed jet height decreases with increasing viscosity (Cheny and Walters, 1996; Castillo-Orozco et al., 2015). Here, we provide the first documented investigation on the influence of deformable fabric thickness χ, area density $\rho'' = \rho_f/A$, where ρ_f and A are the density and area of the fabric sheets respectively, and failure stress σ_f on cavity lengths, splash heights, and hydrodynamic drag coefficients. We present our experimental methods for impactor release, splash visualization, and material property measurements in Section 2. Results and theoretical considerations are presented in Section 3 and the implications of this work discussed in Section 4. We conclude the work in Section 5.

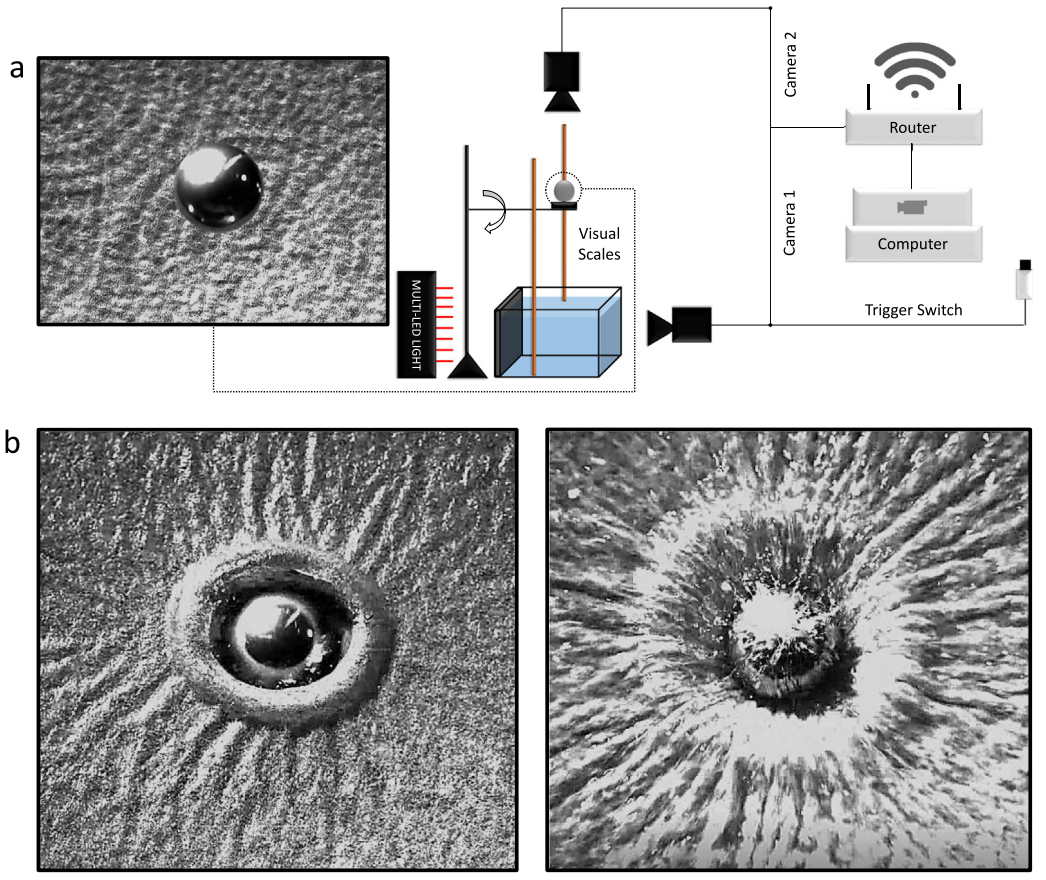

Fig. 2. (a) Schematic of experimental setup. High-speed cameras capture frontal (Photron Mini AX-100) and overhead (Photron Mini UX-100) views with diffuse lighting positioned behind the tank. A wireless router enables multi-camera synchronization. (b) Sphere impact onto punctured (left) and intact (right) fabrics from an overhead view for We = 2688.

2. Methods

2.1. Water entry experiments

Smooth steel hydrophilic spheres of masses $m = 16.6$, 28.6 g and diameters $D = 1.6$, 2.0 cm are released into a 65-L, 36-cm deep aquarium, filled to a depth of 18 cm with tap water. The equilibrium and advancing contact angles on the impactors are $\theta_e = 63^\circ$ and $\theta_a = 68^\circ$, respectively, and are measured photographically using a syringe to deposit water onto the spheres' surface. A pair of meter rulers are mounted vertically inside the tank such that the base of one rests adjacent to the free surface and the second rests on the aquarium floor as seen in Fig. 2a. Square plies of fabric with dimensions 10.5 cm $\times$ 10.5 cm are placed atop the fluid surface such that impacting spheres strike the approximate center of fabrics. Rulers fixed in the plane of impact act as visual scales for calibrating the digital tracking tool (Watson et al., 2019). We clean and dry spheres with 99% isopropyl alcohol before each trial to preclude the influence of surface impurities. Spheres are released from drop heights in the range $h = 10 - 50$ cm by rapidly withdrawing the spheres' supporting platform such that free-fall is purely vertical, irrotational, and generates impact velocity of $U \approx \sqrt{2gh}$, where $g = 9.81$ m/s^2 is the acceleration due to gravity. The sizes of our impactors consume very little fabric area, $1 - 2.8\%$, and permit an impact Weber number range of $430 - 2700$ while remaining well below the threshold of cavity formation for clean surfaces (Duez et al., 2007), $U \approx 8$ m/s. Trials are replicated at least 3 times. Statistical error is included in our plots to show reproducibility of results (Watson et al., 2019). We film impacts with a Photron Mini AX-100 high-speed camera at 2000 frames per second using a 120-mm Nikon lens. In select trials, a Photron Mini UX-100 is added to the experiment to provide a top-down view (Watson et al., 2019). Examples of top-down views for impacts onto punctured and intact fabrics are included in Fig. 2b. We extract position track data and geometric measurements from videos using Tracker, an open source image analysis software.

Table 1
Measured fabric properties and curve fitting correlation values. Curve fitting values for Fabric A corresponds to non-dimensionalized trailing cavity depths κ_t/D as the independent variable, and are thus shown in red to distinguish this uniqueness.

Fabric	χ [μm]	ρ''_{dry} [mg/cm^2]	ρ''_{wet} [mg/cm^2]	$\sigma_{f,dry}$ [MPa]	$\sigma_{f,wet}$ [MPa]	Linear fit R^2	Best fit, α	Best fit R^2
A	80	2.88	23.00	1.20	0.09	0.89	1.63	0.89
B	120	3.24	21.81	1.25	0.33	0.59	1.28	0.59
C	220	5.28	27.19	1.64	0.44	0.90	0.72	0.90
D	40	1.52	1.52	28.84	1.15	0.55	−3.1	0.69

2.2. Material property measurements

We employ several brands of household fabric for surface alteration including: Georgia Pacific Compact Coreless 2-Ply Toilet Paper (Fabric A); Kleenex Trusted Care Facial 2-Ply Tissue (Fabric B); Georgia Pacific Sparkle Professional Series 2-Ply Perforated Roll Paper Towel (Fabric C); and Darice Assorted Colors Tissue Paper (Fabric D). Microscopic images of fabric fibers are shown in the topmost panels of Fig. 1. Failure stresses σ_f are measured with an MTS Criterion 42 tensile tester for dry and wet fabrics (Ishikawa and Chou, 1982; Chou and Ishikawa, 1983; Ishikawa and Chou, 1983; Ishikawa et al., 1985; Dow et al., 1987; Naik et al., 1991; Naik and Shembekar, 1992a,b; Naik, 1995; Shembekar and Naik, 1992; Liu et al., 2009; Zhu et al., 2010). To wet fabrics, we spray 3 cm × 5 cm rectangular sheets with tap water once, using a 60-mL spray bottle, after placement beneath a 10-N load cell. Examples of stress–strain curves are included in the Online Supplement. Dry ρ''_{dry} and wet ρ''_{wet} area densities are measured by weighing fabrics on a Sartorius 225D-1S microbalance. To measure wet mass, we gently rest one edge of fabric rectangles in a small pool of water for 1 min and allow capillary motion to completely wet the material. This method ensures that fabrics are not over-saturated before placement on the analytical balance.

3. Results

We impact four consumer-grade fabrics atop the free surface of a deep aqueous pool with two smooth, free-falling, hydrophilic steel spheres from various drop heights in the range $h = 10 - 50$ cm and compare changes in cavity dimensions, splash heights and drag coefficients with respect to impacts on an unaltered, clean surface (Fig. 1a, Movie S1). Fabric squares measure 10.5 cm per side, a dimension chosen to match the manufactured dimensions of Fabric A. This choice of sheet size permits the penetration of Fabrics A & B, and the entrainment of Fabrics C & D. Fabric properties are measured and shown in Table 1. With sufficiently high impact velocities, spheres puncture fabrics and trigger flow separation; otherwise, fabrics remain intact and are pushed subsurface ahead of descending spheres to form large air-entraining cavities.

3.1. Fabric properties determine cavity shape

We begin by pictorially comparing cavity formation arising from the inclusion of thin, non-woven fabrics atop the fluid surface. Spheres impacting puncturable fabrics such as Fabrics A and B produce no splash crowns and prior to cavity seal (Truscott et al., 2013), the presence of the fabric creates a discontinuity in the cavity wall, such that we may describe two distinct regions (Movie S2), as labeled in Fig. 1. The shallower region is a conical cavity characterized by contact with the fabric, which we denote as the 'fabric cavity.' The deeper region is smoother and vertically-aligned behind the sphere, dubbed the 'trailing cavity.' Fabric A offers the least resistance to puncture across the four test fabrics with $\sigma_{f,wet} = 0.09$ MPa. A typical cavity produced by Fabric A is shown in Fig. 1b, and displays a shallow seal which arises from pressure imbalances close to the free surface (Truscott et al., 2013). The trailing cavity of Fig. 1b remains attached until impact with the container floor. Fabric cavity depths κ_f show minimal variation across the range of Weber number tested for Fabric A (p-value = 0.2256, Table 2) as shown in Fig. 3b. The length of trailing cavities κ_t attached to descending spheres at the moment when the fabric and trailing cavities are sealed from one another likewise shows a weak correlation with Weber number (p-value = 0.2763) as shown in Fig. 3d. For We > 860, trailing cavities pinch-off approximately 20 ms after fabric cavities form, creating deeper seals (Mansoor et al., 2014) as pictured in Fig. 3a.

A typical cavity produced by Fabric B is shown in Fig. 4a, and shares the same cavity regions as Fabric A. However, Fabric B offers greater puncture resistance by way of a greater failure stress, $\sigma_{f,wet} = 0.33$ MPa, nearly 4X that of Fabric A. The impacting sphere forces Fabric B 25% further below the free surface than Fabric A prior to puncture, as shown in the photos of Fig. 4a. The result is a fabric cavity that is on average, twice as deep, creating a longer transition region to the trailing cavity (Movie S3). The depth of the fabric cavity grows mildly with increasing Weber number (p-value < 0.0001), as shown in Fig. 4b. Hydrophilic steel sphere impacts onto intact Fabrics C and D generate time-variant flow separation, ascending splash crowns and greater cavity depths κ_f when compared to their punctured counterparts. This comparison is seen qualitatively in Figs. 5a and 6a, and quantitatively in Figs. 5b and 6b. Despite fabrics obscuring the visibility of flow around spheres, we observe the formation of trailing cavities after pinch-off. As spheres descend, fabrics

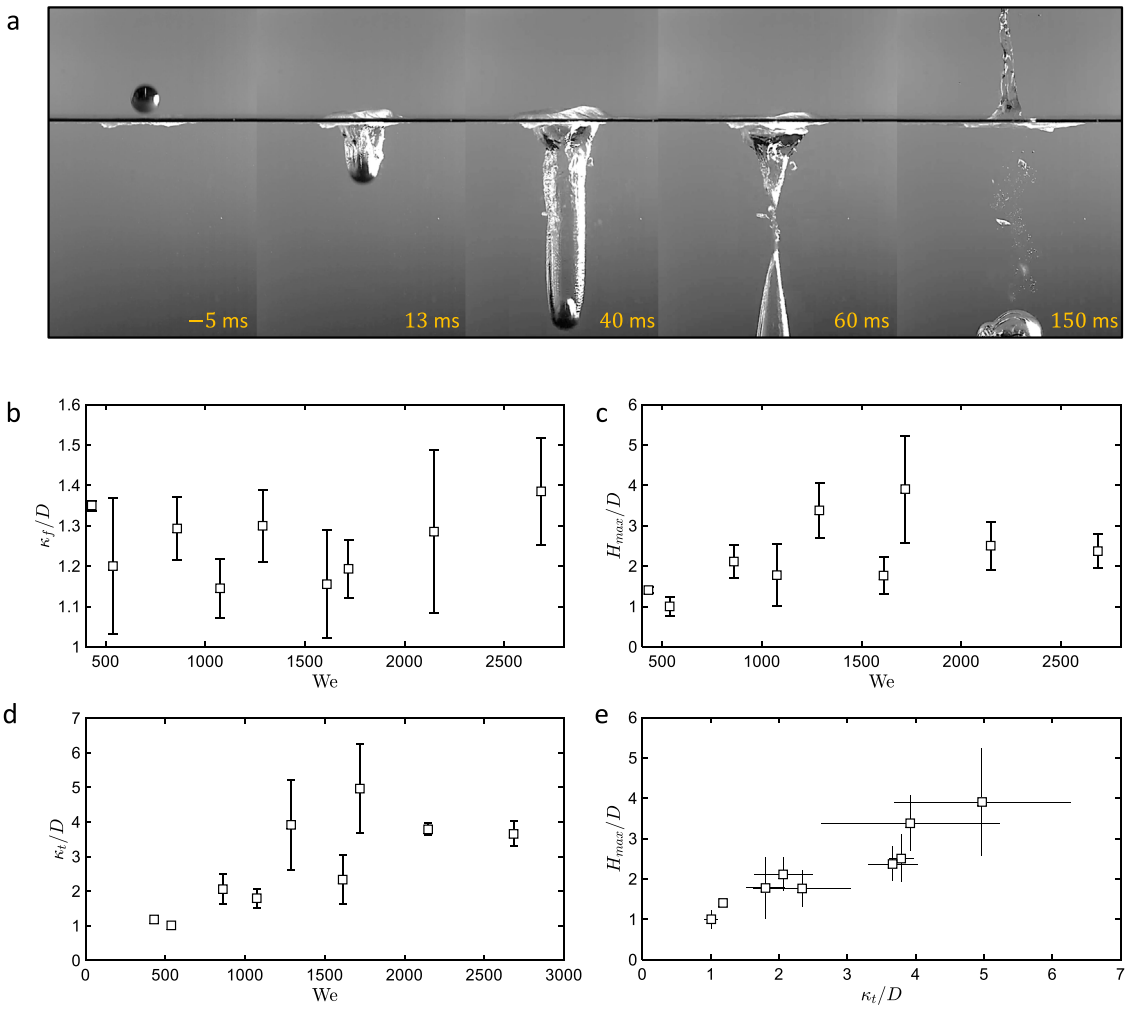

Fig. 3. Fabric A. (a) Time-sequence of a 2-cm hydrophilic steel sphere impacting a single sheet for We = 2688 (Movie S2). Upon impact, a fabric-dependent cavity is formed and collapses near the free surface due to pressure imbalances. As sphere descends, a deeper, smoother, vertically-aligned cavity develops. The trailing cavity again pinches off and adds inertia to the retracting mass of fluid prior to the formation of a Worthington jet. (b) Non-dimensionalized fabric cavity depths κ_f/D versus Weber number We. (c) Non-dimensionalized Worthington jet heights H_{max}/D versus Weber number We. (d) Non-dimensionalized trailing cavity lengths κ_t/D versus Weber number We. (e) Non-dimensionalized Worthington jet heights H_{max}/D versus non-dimensionalized trailing cavity lengths κ_t/D.

Table 2
Single-factor analysis of variance (ANOVA) test for cavity depths and jet heights with respect to Weber number.

Measurements	Fabric	Mean	Standard deviation	Standard error	p-value
κ_f/D	A	1.23	0.1129	0.0652	0.2256
	B	2.20	0.3370	0.1945	9.29×10^{-5}
	C	2.38	0.2617	0.1511	2.40×10^{-5}
	D	2.92	0.2719	0.1570	2.60×10^{-5}
κ_t/D	A	1.51	0.4171	0.2408	0.2763
H_{max}/D	Water	2.42	0.1365	0.0788	4.37×10^{-11}
	A	2.48	0.5841	0.3372	6.39×10^{-4}
	B	3.12	0.5638	0.3255	9.27×10^{-8}
	C	3.45	0.5843	0.3374	1.20×10^{-6}
	D	3.42	0.6214	0.3588	3.05×10^{-6}

are pulled inward and deep seal (Truscott et al., 2013) cavities generated. For such impacts, pinch-off occurs much closer to the spheres, typically greater than 2/3 the distance between spheres and the modified free surface (Movies S4 and S5). In Fig. 7a, we plot non-dimensionalized fabric cavity depths κ_f/D versus We for all fabrics on test.

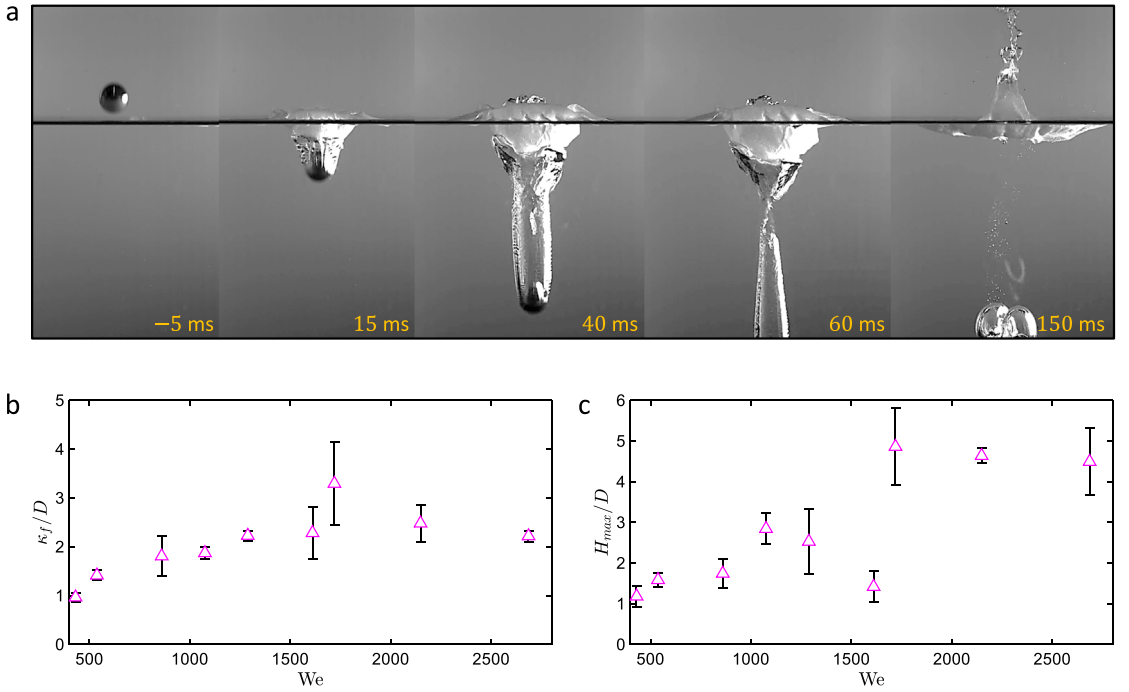

Fig. 4. Fabric B. (a) Time-sequence of a 2-cm hydrophilic steel sphere impacting a single sheet for We = 2688 (Movie S3). Upon impact, a fabric-dependent cavity is formed and collapses near the free surface due to pressure imbalances. As sphere descend, a deeper, smoother, vertically-aligned cavity develops. (b) Non-dimensionalized fabric cavity depths κ_f/D versus Weber number We. (c) Non-dimensionalized Worthington jet height H_{max}/D versus Weber number We.

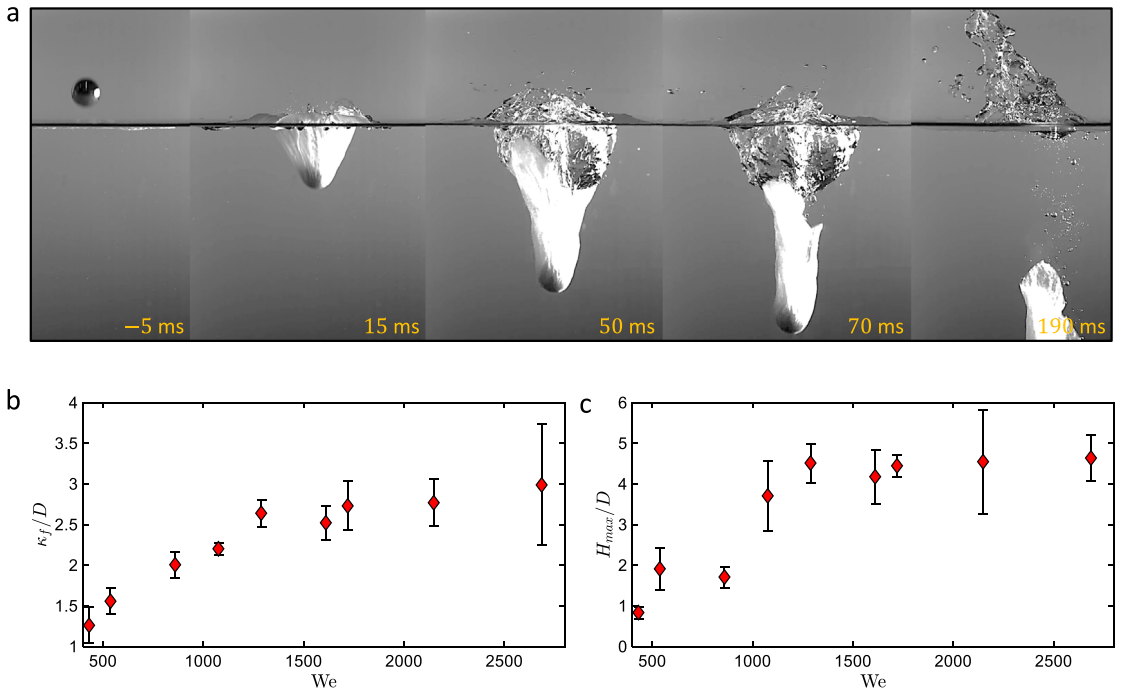

Fig. 5. Fabric C. (a) Time-sequence of a 2-cm hydrophilic steel sphere impacting a single sheet for We = 2688 (Movie S4). Upon impact, fabrics are pulled inward and form deep seal cavities, with pinch-off occurring close to spheres, typically 2/3 the distance between spheres and the modified free surface. (b) Non-dimensionalized fabric cavity depths κ_f/D versus Weber number We. (c) Non-dimensionalized Worthington jet heights H_{max}/D versus Weber number We.

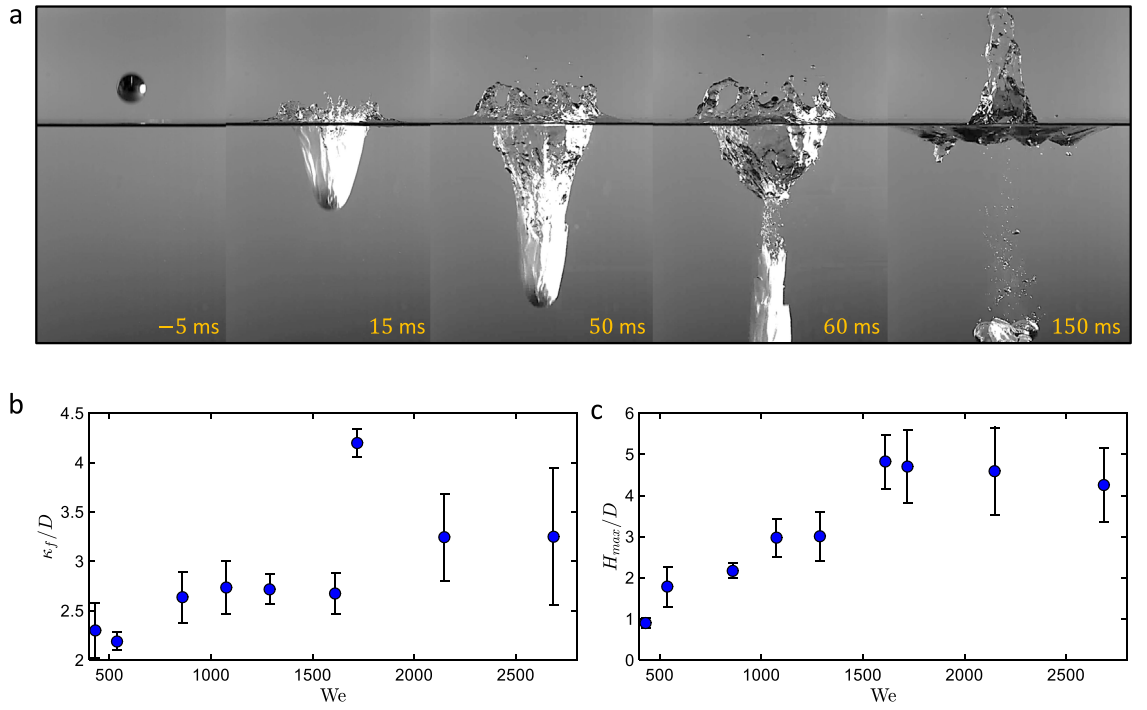

Fig. 6. Fabric D. (a) Time-sequence of a 2-cm hydrophilic steel sphere impacting a single sheet for We = 2688 (Movie S5). Upon impact, fabrics are pulled inward and form deep seal cavities, with pinch-off occurring close to spheres, typically 2/3 the distance between spheres and the modified free surface. (b) Non-dimensionalized fabric cavity depths κ_f/D versus Weber number We. (c) Non-dimensionalized Worthington jet heights H_{max}/D versus Weber number We.

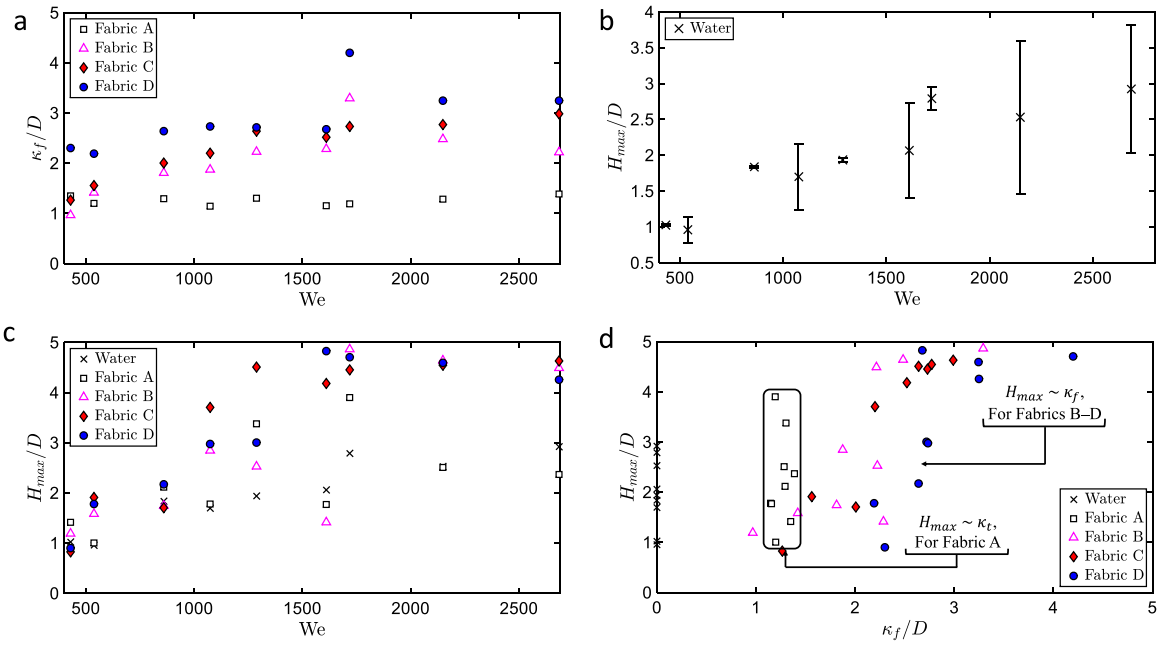

Fig. 7. (a) Aggregated plot of non-dimensionalized fabric cavity depths κ_f/D versus Weber number We for all fabrics on test. (b) Non-dimensionalized Worthington jet heights H_{max}/D versus Weber number We for sphere impacts onto an unmodified free surface. (c) Aggregated plot of non-dimensionalized Worthington jet heights H_{max}/D versus Weber number We for all fabrics on test. (d) Aggregated plot of non-dimensionalized Worthington jet heights H_{max}/D versus non-dimensionalized fabric cavity depths κ_f/D for all fabrics on test.

3.2. Greater puncture resistance promote higher worthington jets

Flow separation from spheres descending through fabric creates air-entraining cavities (Watson et al., 2018). Following the collapse of these cavities, Worthington jets protrude above the free surface. We measure the heights H_{max} of jets and show the inclusion of thin fabrics that are punctured or remain intact amplifies splash heights with respect to an unaltered surface (Fig. 7b), as seen in Fig. 7c. Disaggregated plots with error bars for the data presented in Fig. 7c are provided in Figs. 3c, 4c, 5c, and 6c for Fabrics A–D, respectively. We plot non-dimensionalized splash heights H_{max}/D against non-dimensionalized cavity depths κ_f/D in Fig. 7d for all test fabrics to show the relationship between cavity depths and splash heights changes with fabric strength. Disaggregated plots are included in the Online Supplement. Generally, as fabric failure stress σ_f increases, so does κ_f for a given H_{max} as the deformable interface becomes more difficult to penetrate for larger values of σ_f. The threshold for puncture for our impactors within the test range of We lies between the strengths of Fabrics B and C, $\sigma_{f,wet} = 0.33$ and 0.44 MPa, respectively.

We rationalize the trends for H_{max}/D in Fig. 7d by considering a conical cavity that seals behind a descending sphere, ultimately collapsing to produce a Worthington jet of diameter D_j. A cavity of diameter D_c and volume $\forall_c \sim D_c^2\kappa_f$ is subject to a buoyant force $F_{B,c} \sim \rho g \forall_c$, and upon collapse experiences boundary work $W_{B,c} \sim F_{B,c}\kappa_f$. The influence of surface tension on cavity collapse is negligible given that Bond number $Bo = \Delta\rho g\kappa_f^2/\sigma \gg 1$, where $\Delta\rho$ is the difference between water and air density. As the cavity retracts, the work of the collapsing cavity is converted to gravitational potential energy in the jet $W_{B,c} \sim E_{p,j} \sim \rho g \forall_j H_{max}$, where $\forall_j \sim D_j^2 H_{max}$ is the volume of the protruding fluid (Watson et al., 2018). For simplicity, we assume geometric similarity of Worthington jets across impact trials. We neglect viscous dissipation during cavity collapse and jet ascension given $Re > 26{,}000$. Therefore we may write $\rho g D_c^2\kappa_f^2 \sim \rho g D_j^2 H_{max}^2$. Experience mandates the diameter of a disturbance in a compliant fluid surface is approximately equal to the diameter of the ensuing response, $D_c \sim D_j$. Accordingly,

$$H_{max} \sim \kappa_f. \tag{1}$$

We fit Eq. (1) to our experimental data and find linear fit correlation values in the range $R^2 = 0.69 - 0.88$ for Fabrics B–D. Individual correlation values are given in Table 1 alongside best fit exponents according to $H_{max} \sim \kappa_f^{\alpha}$. We note an insignificant change in correlation values when the exponent α deviates from unity for Fabrics B and C. By contrast, $\alpha = -3.1$ for Fabric D, a stark deviation from unity, producing a small correlation value improvement of 0.14. The cause for this contrast is unknown, but it is noteworthy that Fabric D is anomalous in ρ''_{wet} and $\sigma_{f,dry}$ compared to the other fabrics.

Fabric A does not fit well to the scaling argument given in Eq. (1), $\alpha = -72$, because the collapse and ascension of trailing cavities is the primary contributor to Worthington jet creation (Fig. 3e, Movie S2). For impacts onto Fabric A, the work done by cavity collapse scales with κ_t, and using the aforementioned arguments, the jet height for impacts through Fabric A obeys,

$$H_{max} \sim \kappa_t. \tag{2}$$

We fit Eq. (2) to our experimental data and find linear fit correlation value $R^2 = 0.89$ for Fabric A. For non-cavity producing impacts (Watson et al., 2018), the gravitational potential energy of a sphere of density ρ_s and volume $\forall_s$ is converted to gravitational potential in the jet, $\rho_s \forall_s g h \sim \rho \forall_j g H_{max}$. We rationalize $\forall_j \sim \forall_s$ by noting that the volume of fluid displaced by the sphere should be that thrown airborne into the jet. Thus, the heights of Worthington jets arising from impacts with free surface conditions are more suitably described by

$$H_{max} \sim h, \tag{3}$$

as shown in Fig. 7d and verified in previous work (Watson et al., 2018). Best fits and linear fits as discussed above are shown in Fig.S2.

3.3. Fabrics amplify and attenuate hydrodynamic drag

To compare the hydrodynamic drag force induced by test fabrics, we fix drop height $h = 50$ cm such that $U = 3.13$ m/s and track the center of mass of 2-cm steel spheres, as seen in Fig. 8a. Position track data is initialized ($t = 0$ s) when spheres strike the fluid surface and terminated just before impact with the floor of the liquid pool. A force balance for a sphere of mass m falling vertically into a quiescent liquid bath is given by Watson et al. (2018)

$$F_D = mg - (m + m_a)\, a - F_B - F_\sigma, \tag{4}$$

where $F_D = \pi\rho U^2 C_D D^2/8$ is the drag force acting on the sphere, a is the linear acceleration of the sphere, $m_a = \pi\rho D^3 C_m/6$ is the added mass, accounting for the effect of accelerating fluid by the falling sphere (Watson et al., 2018), and $C_m = 0.5$ is the added mass coefficient, treated as a constant across all cases (Aristoff and Bush, 2009; Aristoff et al., 2010). We note that while C_m increases from zero at impact (Aristoff and Bush, 2009; Aristoff et al., 2010), our model is not highly sensitive to this change given $m/m_a \sim O(10)$, producing a 13% variance in the calculated value of C_D over a range of $C_m = 0 - 1$. Buoyancy force (Watson et al., 2018) is given by $F_B = \rho g(\frac{\pi}{6}D^3 + A(y)y)$, where y is the position track and $A(y)$

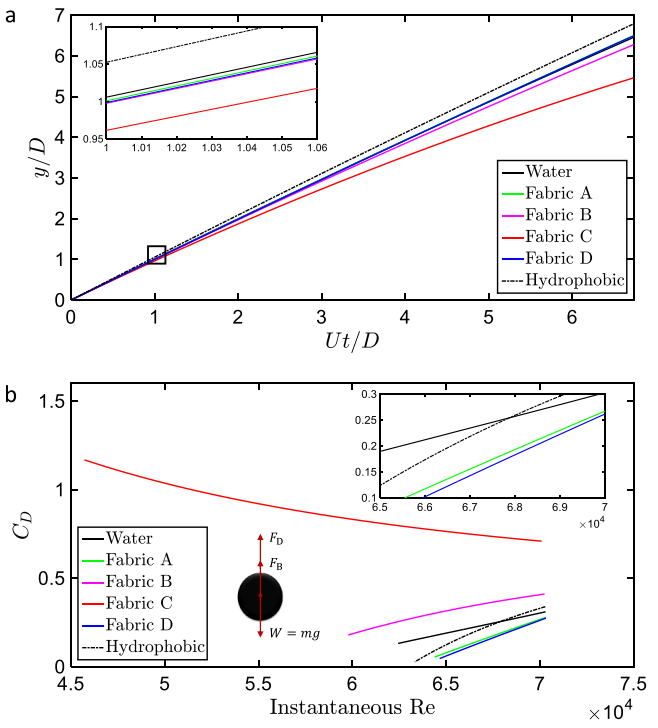

Fig. 8. (a) Non-dimensionalized vertical position versus dimensionless time. Trajectories are smoothed with a Savitzky–Golay filter to remove the effects of experimental error. (b) The relation between hydrodynamic drag coefficient C_D and instantaneous Reynolds number Re.

is cross-sectional area of the sphere at the plane of flow separation (Watson et al., 2018). For further simplification, we treat $A(y)$ as constant by assuming separation at the equator such that $F_B = \rho g \pi (\frac{D^3}{6} + \frac{D^2}{4} y)$. We may neglect the force due to surface tension $F_\sigma = \sigma D$ in the range of Weber number on test. Thus, Eq. (4) can be rewritten as

$$\frac{du}{dt} = \frac{mg}{m'} - \frac{\rho g \pi D^2}{8m'} \left(\frac{4}{3} D + 2y + \frac{C_D}{g} u^2 \right), \tag{5}$$

where $m' = m + m_a$. Position track data is smoothed with a Savitzky–Golay filter (Krishnan and Seelamantula, 2013) to remove the effects of experimental error prior to numerical differentiation to obtain temporal velocity $u(t)$, and then smoothed once more prior to the final differentiation to obtain acceleration $a(t)$. The smoothing filter is a generalized moving average spanning the entire dataset with coefficients determined by an unweighted linear least-squares regression and a polynomial model of specified degree. Figures S3–S6 in the Online Supplement demonstrate the effect of various filtering options on experimental and differentiated data, and C_D. Filter options were chosen to maintain the physical integrity of the data throughout processing. Other smoothing and differentiation techniques are available, such as that provided by Epps et al. (2010), but such techniques did not provide physically relevant data due to limitations in measuring sphere position precisely when shrouded by fabric.

A numerical solution of Eq. (5) provides values of C_D for each fabric in the range of instantaneous Reynolds number $\mathrm{Re} = \rho D u(t)/\mu = 45{,}000 - 71{,}000$, where $\mu = 8.90 \times 10^{-4}$ Pa s is the dynamic viscosity of water, as plotted in Fig. 8b. As a further comparison of drag coefficients C_D imposed by each fabric, consider the following values for Re = 70,000: 0.30 – free surface; 0.27 – Fabric A; 0.40 – Fabric B; 0.68 – Fabric C; and 0.27 – Fabric D. The increase in C_D from Fabric A through C corresponds with increasing ρ''_{wet} and $\sigma_{f,wet}$. Though the most resistant to puncture, Fabric D's relatively low ρ''_{wet} allows the sphere to enter against relatively little inertial resistance.

Our calculated drag coefficients $C_D \approx 0.1 - 0.3$ for clean water align with those of steadily-translating spheres in the same Reynolds number range, $\mathrm{Re} \approx 10^4 - 10^5$, and have a positive slope with increasing Re (Maxworthy, 1965, 1969; Achenbach, 1972; Lofquist and Purtell, 1984). With respect to clean water producing non-cavity forming impacts Fabric A (punctured) and Fabric D (intact) reduce drag force during descent as seen in Fig. 8b. This surprising result may be interpreted in the context of the work of Truscott et al. (2012.), who explored the unsteady forces on free-falling hydrophilic and hydrophobic spheres traversing the liquid bath. In their study, non-cavity forming impacts by 2.54-cm steel spheres with Re = 12,500 – 87,500 and entry velocity $U = 3.43$ m/s, had higher drag coefficients $C_D = 0.20 - 1.00$ than their cavity forming ($\theta_e = 120°$) counterparts $C_D = 0.35 - 0.40$ due to pressure recovery in the wake and the initiation of vortex shedding (Truscott et al., 2012.). Although the inertial resistance or mechanical failure of the fabric

acts to increase drag, the suppression of trailing vortices by the air-entraining cavity results in a net reduction in entry resistance.

4. Discussion

This study shows that hydrophilic steel spheres impacting a liquid bath modified by the placement of thin, non-woven fabric sheets atop the fluid surface experience fabric dependent cavity shapes and Worthington jet heights. Splashes from spherical projectiles colliding with the compliant fabric interface generate greater jet heights compared to impacts with an unmodified free surface. In contrast to jet amplification, impacts onto punctured fabric sheets attenuate splash crowns. Intact impacts amplify splash crowns as fabrics ride ahead of spheres during descent through the pool. Below the surface, cavity-producing impacts induced by fabric sheets are unable to generate smooth, uniform cavity walls normally seen for the water entry of smooth hydrophobic spheres (Truscott et al., 2013) (Movie S6). Instead, surface waves appear on cavity walls due to the inherent jaggedness that accompanies torn fabric, creating localized variation in flow separation, and confirming the coupling of fabric properties to cavity behavior. This inherent jaggedness is a likely cause of the random, and in some places, severe variation in splash characteristics of Fig. 7.

The chosen size and shape of our impacted fabrics determine their status as punctured or intact, and the ability of the impactor to partially or fully entrain the fabric. If the fabrics were infinite in size, punctured Fabrics A & B would remain so, while Fabrics C & D may become punctured at some value of We in our experimental range. The status of Fabrics C & D as intact is reliant on their compliance. We do not expect changing the profile of fabric, i.e. to a circle (Movie S7), to substantially influence puncture or cavity dynamics, but instead expect changes to fabric buckling (Fig. 2b) at impact. The absorbency of fabrics on test is accounted for by the area density ρ'' and failure stress σ_f as shown in Table 1. As such, the use of non-wetting fabrics would provide a greater range of ρ'' and σ_f that remain unchanged when wet.

The complex nature of fabric buckling and tearing as shown by the collision in Fig. 2b, makes the prediction of Worthington jet alignment with the vertical axis intractable. Jet direction variance from vertical is reflected in the experimental noise of Fig. 7. An example of jet deviation from vertical can be seen in Movie S3. To further highlight the role of buckling on splash directionality, we substitute fabrics with thin, layers of ice. The falling sphere punches an opening in the ice, tripping flow separation, followed by a vertically ascending jet with no horizontal velocity, likely due to the absence of buckling during the brittle fracture of the interface (Movie S8). In contrast to ice, the physical properties of the interface will, in many cases, not be isotropic. While all our non-woven fabrics exhibit isotropic properties, woven fabric weaves can provide anisotropic stiffness (Pochiraju and Chou, 1999; Dai et al., 2003; Kovar and Gupta, 2009) and substantially different buckling patterns. Thus, the relation between fabric buckling and splash dynamics is an area requiring further investigation.

The square profile of our fabrics ensures non-axisymmetric entry of intact fabrics because the corners trail furthest behind the impactor. Deviation from perfectly centric impacts, which are inevitable, will likewise produce variations in buckling, which we do not expect to significantly bias results. We justify this notion by observation of Fig. 5a (Movie S4) and Fig. 6a (Movie S5), in which the non-axisymmetric buckling does not appear to have a large effect on splash features, such as the crown. We add robustness against eccentric impacts by repeating trials three times and choosing impactors with diameters $\leq$ 19% the length of our fabric squares. At the extreme of eccentricity, spheres strike edge of the fabric, producing localized half-cavities at low entry velocities. We drop a 2-cm Delrin sphere with mass $m = 7.7$ g from $h = 10$ cm and ensure water entry along the fabric edge (Movie S9). Upon impact, flow separation is tripped only along the portion contacted by fabric. The partial obstruction by compliant films is thus another means to tune splash dynamics that requires further investigation.

5. Conclusion

Punctured fabrics create two cavity regions as the impactor descends. The shallower cavity is approximately cone-shaped, while the deeper cavity is elongated and has a diameter approximately equal to impactor width. The shape of cavities induced by punctured fabrics is a result of tripping flow separation at velocities which would otherwise not produce air-entrainment. Punctured fabrics remain near the free surface, suppressing the splash crown, but allowing passage of a Worthington jet whose height increases with Weber number. Intact fabrics create cavities by veiling the descending impactor, amplifying the splash crown and producing Worthington jets which likewise increase in height with Weber number. Generally, increases in fabric wet area density and puncture resistance promote greater air-entraining cavity depths. The collapse of deeper cavities produces higher Worthington jets. Fabrics with high area-density slow impactor speed via dominant inertial effects, but when compared to impacts that produce no cavities, air-entraining cavities reduce drag, as evidenced by the employment of lightweight and easily punctured fabrics. Splash height and impactor motion may thus be tuned by fabric properties.

Declaration of competing interest

The authors declare that they have no known competing financial interests or personal relationships that could have appeared to influence the work reported in this paper.

CRediT authorship contribution statement

Daren A. Watson: Conceptualization, Investigation, Methodology, Project administration, Formal analysis, Writing - review & editing. **Chris J. Souchik:** Data curation, Visualization. **Madison P. Weinberg:** Data curation, Visualization. **Joshua M. Bom:** Data curation, Visualization. **Andrew K. Dickerson:** Conceptualization, Funding acquisition, Investigation, Methodology, Project administration, Formal analysis, Writing - review & editing.

Acknowledgments

We would like to acknowledge the NSF (CBET-1941341) for financial support, and Nicholas Smith, Jeremy Stephen, Amy Lebanoff, and Alexander Tao for experimental support. We also thank David Richardson from the NMR Facility and Cryogenic Services at the University of Central Florida for providing liquid nitrogen.

Appendix A. Supplementary data

Supplementary material related to this article can be found online at https://doi.org/10.1016/j.jfluidstructs.2020.102907. See supplementary material for 9 movies and a supplementary document. The document contains descriptions of the movies and additional plots showing stress–strain curves used for obtaining dry $\sigma_{f,dry}$ and wet $\sigma_{f,wet}$ failure stresses for each fabric tested. We also include disaggregated plots with linear and exponent fits to show the relation between non-dimensionalized splash heights H_{max}/D and non-dimensionalized cavity depths κ_f/D for increasing fabric strength.

References

Achenbach, E., 1972. Experiments on the flow past spheres at very high reynolds numbers. J. Fluid Mech. 54 (3), 565–575.
Aristoff, J., Bush, J., 2009. Water entry of small hydrophobic spheres. J. Fluid Mech. (ISSN: 00221120) 619, 45–78.
Aristoff, J., Truscott, T., Techet, A., Bush, J., 2010. The water entry of decelerating spheres. Phys. Fluids (ISSN: 10706631) 22 (3).
Bodily, K.G., Carlson, S.J., Truscott, T.T., 2014. The water entry of slender axisymmetric bodies. Phys. Fluids (ISSN: 1089-7666) 26 (7), 072108. http://dx.doi.org/10.1063/1.4890832.
Castillo-Orozco, E., Davanlou, A., K. Choudhury, P., Kumar, R., 2015. Droplet impact on deep liquid pools: rayleigh jet to formation of secondary droplets. Phys. Rev. E 92.
Che, Z., Matar, O.K., 2018. Impact of droplets on immiscible liquid films. Soft Matter 14 (9), 1540–1551.
Cheny, J., Walters, K., 1996. Extravagant viscoelastic effects in the worthington jet experiment. J. Non-Newton. Fluid Mech. (ISSN: 0377-0257) 67 (Supplement C), 125–135, Papers Presented at the Workshop on 'Unresolved Experimental Dilemmas in the Dynamics of Complex Fluids'.
Chou, T.-W., Ishikawa, T., 1983. One-dimensional micromechanical analysis of woven fabric composites. AIAA J. 21 (12), 1714–1721.
Cossali, G.E., Marengo, M., Coghe, A., Zhdanov, S., 2004. The role of time in single drop splash on thin film. Exp. Fluids (ISSN: 1432-1114) 36 (6), 888–900.
Dai, X., Li, Y., Zhang, X., 2003. Simulating anisotropic woven fabric deformation with a new particle model. Text. Res. J. 73 (12), 1091–1099.
Dow, N.F., Ramnath, V., Rosen, B.W., 1987. Analysis of woven fabrics for reinforced composite materials.
Duck-Gyu, L., Ho-Young, K., 2008. Impact of a superhydrophobic sphere onto water. Langmuir (ISSN: 07437463) 24 (1), 142–145.
Duclaux, V., Caille, F., Duez, C., Ybert, C., Bocquet, L., Clanet, C., 2007. Dynamics of transient cavities. J. Fluid Mech. (ISSN: 1469-7645) 591, http://dx.doi.org/10.1017/s0022112007007343.
Duez, C., Ybert, C., Clanet, C., Bocquet, L., 2007. Making a splash with water repellency. Nat. Phys. (ISSN: 17452473) 3 (3), 180–183.
Epps, B.P., Truscott, T.T., Techet, A.H., 2010. Evaluating derivatives of experimental data using smoothing splines. In: Proceedings of Mathematical Methods in Engineering International Symposium. MMEI, Lisbon Portugal.
Glasheen, J., McMahon, T., 1996. Vertical water entry of disks at low froude numbers. Phys. Fluids 8 (8), 2078–2083.
Hu, D.L., Chan, B., Bush, J.W.M., 2003. The hydrodynamics of water strider locomotion. Nature (ISSN: 00280836) 424 (6949), 663–666.
Ishikawa, T., Chou, T.-W., 1982. Stiffness and strength behaviour of woven fabric composites. J. Mater. Sci. 17 (11), 3211–3220.
Ishikawa, T., Chou, T.-W., 1983. Nonlinear behavior of woven fabric composites. J. Compos. Mater. 17 (5), 399–413.
Ishikawa, T., Matsushima, M., Hayashi, Y., Chou, T.-W., 1985. Experimental confirmation of the theory of elastic moduli of fabric composites. J. Compos. Mater. 19 (5), 443–458.
Kim, N., Park, H., 2019. Water entry of rounded cylindrical bodies with different aspect ratios and surface conditions. J. Fluid Mech. 863, 757–788.
Kovar, R., Gupta, B.S., 2009. Study of the anisotropic nature of the rupture properties of a plain woven fabric. Text. Res. J. 79 (6), 506–516.
Krishnan, S.R., Seelamantula, C.S., 2013. On the selection of optimum savitzky-golay filters. IEEE Trans. Signal Process. (ISSN: 1053-587X) 61 (2), 380–391.
Kubota, Y., Mochizuki, O., 2011. Influence of head shape of solid body plunging into water on splash formation. J. Vis. (ISSN: 1875-8975) 14 (2), 111–119.
Li, D., Zhang, J., Zhang, M., Huang, B., Ma, X., Wang, G., 2019. Experimental study on water entry of spheres with different surface wettability. Ocean Eng. (ISSN: 0029-8018) 187, 106123. http://dx.doi.org/10.1016/j.oceaneng.2019.106123.
Liu, Y., He, H., Yao, J., 2009. Mathematical model for knitted bodywear based on fabric elasticity [j]. J. Text. Res. 4.
Lofquist, K.E., Purtell, L., 1984. Drag on a sphere moving horizontally through a stratified liquid. J. Fluid Mech. 148, 271–284.
Mansoor, M.M., Marston, J.O., Vakarelski, I.U., Thoroddsen, S.T., 2014. Water entry without surface seal: extended cavity formation. J. Fluid Mech. 743, 295–326.
Maxworthy, T., 1965. Accurate measurements of sphere drag at low reynolds numbers. J. Fluid Mech. 23 (2), 369–372.
Maxworthy, T., 1969. Experiments on the flow around a sphere at high reynolds numbers. J. Appl. Mech. 36 (3), 598–607.
May, A., 1951. Effect of surface condition of a sphere on its water-entry cavity. J. Appl. Phys. (ISSN: 00218979) 22, 1219–1222.
Naik, R.A., 1995. Failure analysis of woven and braided fabric reinforced composites. J. Compos. Mater. 29 (17), 2334–2363.
Naik, N., Shembekar, P., 1992a. Elastic behavior of woven fabric composites: i—lamina analysis. J. Compos. Mater. 26 (15), 2196–2225.
Naik, N., Shembekar, P., 1992b. Elastic behavior of woven fabric composites: iii—laminate design. J. Compos. Mater. 26 (17), 2522–2541.
Naik, N., Shembekar, P., Hosur, M., 1991. Failure behavior of woven fabric composites. J. Compos. Technol. Res. 13 (2), 107–116.

Ogawa, A., Utsuno, K., Mutou, M., Kouzen, S., Shimotake, Y., Satou, Y., 2006. Morphological study of cavity and Worthington jet formations for Newtonian and non-Newtonian liquids. Part. Sci. Technol. (ISSN: 02726351) 24 (2), 181–225.
Pochiraju, K., Chou, T.-W., 1999. Three-dimensionally woven and braided composites. i: A model for anisotropic stiffness prediction. Polym. Compos. 20 (4), 565–580.
Shembekar, P., Naik, N., 1992. Elastic behavior of woven fabric composites: ii—laminate analysis. J. Compos. Mater. 26 (15), 2226–2246.
Shin, J., McMahon, T.A., 1990. The tuning of a splash. Phys. Fluids A 2 (8), 1312–1317.
Speirs, N.B., Pan, Z., Belden, J., Truscott, T.T., 2018. The water entry of multi-droplet streams and jets. J. Fluid Mech. 844, 1084–1111.
Techet, A., Truscott, T., 2011. Water entry of spinning hydrophobic and hydrophilic spheres. J. Fluids Struct. (ISSN: 0889-9746) (5–6), 716.
Thoroddsen, S.T., Etoh, T.G., Takehara, K., Takano, Y., 2004. Impact jetting by a solid sphere. J. Fluid Mech. 499, 139–148.
Truscott, T.T., 2009. Cavity dynamics of water entry for spheres and ballistic projectiles. (Doctor of Philosophy). Massachusetts Institue of Technology.
Truscott, T.T., Epps, B.P., Belden, J., 2013. Water entry of projectiles. Annu. Rev. Fluid Mech. (ISSN: 00664189) 46, 355–378.
Truscott, T., Epps, B., Techet, A., 2012.. Unsteady forces on spheres during free-surface water entry. J. Fluid Mech. (ISSN: 00221120) 704, 173–210.
Truscott, T., Techet, A., 2009. Water entry of spinning spheres. J. Fluid Mech. (ISSN: 00221120) 625, 135–165.
Ueda, Y., Iguchi, M., 2012. Water entry of stripe-coated hydrophobic circular cylinders. J. Vis. 15 (1), 33–35.
Watson, D.A., Stephen, J.L., Dickerson, A.K., 2018. Jet amplification and cavity formation induced by penetrable fabrics in hydrophilic sphere entry. Phys. Fluids 30 (8), 082109.
Watson, D.A., Stephen, J.L., Dickerson, A.K., 2019. Impacts of free-falling spheres onto a deep liquid pool with altered fluid and impactor surface conditions. J. Vis. Exp. 144, e59300.
Worthington, A.M., 1908. A study of splashes.
Worthington, A.M., Cole, R.S., 1897. Impact with a liquid surface studied by the aid of instantaneous photography. Phil. Trans. R. Soc. A (ISSN: 02643952) 137.
Worthington, A.M., Cole, R.S., 1900. Impact with a liquid surface studied by the aid of instantaneous photography. paper ii. Phil. Trans. R. Soc. A (ISSN: 02643952) 175.
Zhao, S., Wei, C., Cong, W., 2016. Numerical investigation of water entry of half hydrophilic and half hydrophobic spheres. Math. Probl. Eng. 2016, 1–15.
Zhu, D., Mobasher, B., Rajan, S.D., 2010. Dynamic tensile testing of kevlar 49 fabrics. J. Mater. Civ. Eng. 23 (3), 230–239.